PROBING INTRACAVITY PLASMA DYNAMICS WITH HIGHER-ORDER TRANSVERSE MODES

by

Brian C. Goodell

A Thesis Submitted to the Faculty of the

COLLEGE OF OPTICAL SCIENCES

In Partial Fulfillment of the Requirements
For the Degree of

MASTER OF SCIENCE

In the Graduate College

THE UNIVERSITY OF ARIZONA

2017

STATEMENT BY AUTHOR

The thesis titled *Probing Intracavity Plasma Dynamics with Higher-Order Transverse Modes* prepared by *Brian C. Goodell* has been submitted in partial fulfillment of requirements for a master's degree at the University of Arizona and is deposited in the University Library to be made available to borrowers under rules of the Library.

Brief quotations from this thesis are allowable without special permission, provided that an accurate acknowledgement of the source is made. Requests for permission for extended quotation from or reproduction of this manuscript in whole or in part may be granted by the head of the major department or the Dean of the Graduate College when in his or her judgment the proposed use of the material is in the interests of scholarship. In all other instances, however, permission must be obtained from the author.

SIGNED: *Brian C. Goodell*

APPROVAL BY THESIS DIRECTOR

This thesis has been approved on the date shown below:

_____

R. Jason Jones
Professor of Optical Physics

Defense date
June 15, 2017

DEDICATION

To Mom, Dad, Kylie, and Chris. Thank you for your love and support.

TABLE OF CONTENTS

LIST OF FIGURES

LIST OF TABLES

ABSTRACT

Extreme ultraviolet (XUV) frequency combs exhibit promise for enabling high-precision spectroscopic measurements of myriad chemical species for the first time. Coherent XUV radiation can be generated through high harmonic generation (HHG) in femtosecond enhancement cavities. HHG efficiency is limited by nonlinear phase shifts induced by residual intracavity plasma. The goal of this work is to gain insight regarding plasma dynamics in order to allay the detrimental effects of plasma interactions. Our approach is to conduct simulations of cavity pump-probe experiments by probing with higher-order transverse modes. We propose methods for estimating spatial plasma profiles, gas jet velocities, and the plasma recombination coefficient based on measurements of plasma-induced phase shifts. Beam distortion due to plasma interaction is analyzed and used as another reference for plasma dynamics.

CHAPTER 1: BACKGROUND

1.1 XUV Frequency Comb Development

Spectroscopy is an indispensable method for understanding light-matter interactions, atomic and molecular chemistry, and quantum effects. The development of synchrotron sources has pushed the limits of spectroscopic experiments by offering high-power beams over a broad range of wavelengths. Nevertheless, the spectral resolution of synchrotrons in the extreme ultraviolet region (XUV) is orders of magnitude lower than that of the visible spectrum, and the large facilities that house these sources are limited in accessibility. In contrast, the advent of phase-coherent femtosecond frequency combs revolutionized the field of precision spectroscopy and gave rise to sub-cycle attosecond science [1]. While extensive investigations have been performed using frequency combs in the visible and infrared, accurate measurements of transitions in the vacuum ultraviolet (VUV) and XUV have remained elusive. Recent progress in extending frequency combs to lower wavelengths exhibits potential for uniting XUV science and precision spectroscopy to enable a vast array of significant transitions to be analyzed for the first time with unparalleled accuracy. Such a breakthrough would advance knowledge in innumerable fields, including astrophysics. For example, databases of precision spectroscopic measurements would satisfy a need in the areas of planetary atmosphere chemistry, interstellar medium chemistry, and cosmology for standards with which to compare telescope data [2].

Initial results to develop XUV frequency combs have been promising. Our group previously achieved record VUV and XUV power levels of 10-77 μW over 50-150 nm through high harmonic generation (HHG) in a femtosecond enhancement cavity [3]. Even higher powers can now be realized by our Yb-doped fiber laser system. Other researchers have measured

transitions in Ne and Ar for the first time using an XUV frequency comb [4]. Complex molecules are more difficult to measure using a single comb, as the entire transition must occur between the spacing of two modes. Additionally, diffraction-based instruments such as gratings lack the resolving power to isolate individual frequency modes. Our unique approach to solve these problems has been to employ dual-frequency comb spectroscopy [5], a technique that has been successfully demonstrated in the infrared region [6]. We overlap two combs with slightly different repetition rates to produce a radio frequency spectrum of heterodyne beats. Each mode corresponds to a distinct radio frequency so that all comb components can be detected simultaneously. Trials with the 3rd harmonic have succeeded in discriminating individual beat notes and maintaining stability.

1.2 XUV Frequency Comb Applications

Molecular hydrogen (H_2) and the molecular hydrogen ion (H_2^+) are the simplest molecules in existence and consequently serve as benchmarks for quantum modeling. The ionization potential (IP) of H_2 is presently known within 10 MHz of uncertainty [7]. In comparison, the energy required to ionize high-n Rydberg states of H_2 is known to an uncertainty of less than 100 kHz [8]. Therefore, accurately determining the transitions of H_2 from the ground state to Rydberg states would reduce the uncertainty of the IP by orders of magnitude. These transitions occur in the XUV near 79 nm, which could reasonably be probed by our dual-comb system to a precision limited only by Doppler broadening. Reducing uncertainty for the IP of H_2 would assist in refining quantum simulations of molecules. In theory, measuring the IP to a sufficient degree of accuracy could provide more precise values for fundamental constants, such as the Rydberg constant and proton-to-electron mass ratio μ [9]. Evidence suggests that constants

such as μ may vary on cosmological time scales [10]. Comparing the IP of H_2 today with absorption spectra from distant stars would allow any time evolution of μ to be identified.

Another appealing species for spectroscopic analysis is the thorium isotope ^{229}Th. While nuclear transitions typically occur on the order of keV or MeV, recent indirect measurements posit that ^{229}Th undergoes an isomeric nuclear transition of only 7.8 ± 0.5 eV [11]. This exceptionally low-energy transition could, in principle, be probed by our dual-frequency comb system. Accomplishing this momentous feat would mark the first direct measurement of a nuclear transition by laser spectroscopy. A precision measurement of this transition would also make ^{229}Th an attractive candidate for frequency and time standards. As a time standard, a ^{229}Th nuclear clock would improve the efficiency of the Global Positioning System (GPS), deep-space navigation systems, and Internet functions that require time-synchronization. Unlike atomic clocks which require a vacuum chamber, a nuclear clock could consist of ^{229}Th embedded in a stable crystal lattice [12], thereby increasing stability by reducing Doppler broadening. Nuclear time standards could also be used to detect minor fluctuations in the gravitational force induced by materials of varying density in the earth, permitting remote sensing for mining applications and seafloor mapping.

1.3 HHG, Residual Plasma, and Nonlinear Cavity Response

We generate coherent XUV radiation by performing HHG with a xenon gas target inside a femtosecond enhancement cavity (Fig. 1.1). A complete description of HHG is complex and calls for fully quantum modeling of nonlinear optics [13]. More often, a semi-classical model is sufficient to describe the process [14], as is the case with this work. When an intense laser pulse (~10^{13} W/cm^2) is incident on a gas target, the strong electric field can suppress the Coulomb

barrier to permit ionization through electron tunneling (Fig. 1.2). Ionization can thereby occur for photon energies $\hbar\omega$ much lower than the ionization potential. Monatomic gases are typically preferred as the ionization mechanisms of atoms are simpler than those of molecules. Following ionization, the free electron accelerates away from the parent ion under the influence of the electric field. After half of an optical cycle, the field changes direction to drive the electron back toward the parent ion. If the electron collides with the ion, recombination can occur, emitting radiation at harmonic frequencies of the fundamental beam. Acceleration and recombination events occur twice for every cycle of the driving laser so that harmonics are separated by a frequency 2ω. As a result, only odd-numbered harmonics are possible.

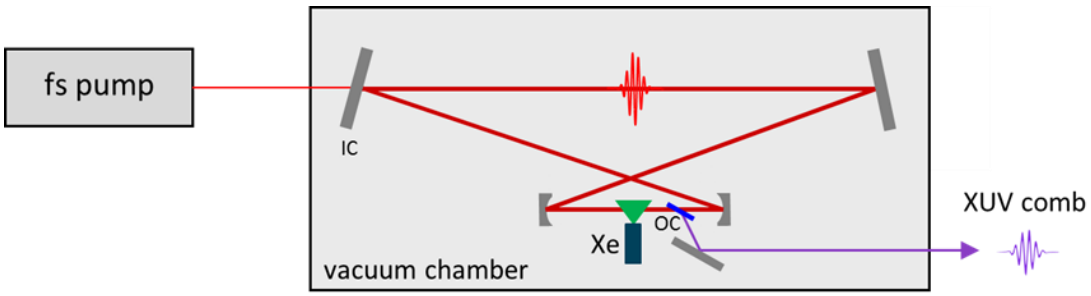

Figure 1.1. Schematic of intracavity HHG. The pump is an infrared femtosecond frequency comb. Numerous pulses circulate through the cavity and constructively interfere to enhance the power. Curved mirrors focus the beam to a small spot size to maximize intensity. A xenon gas jet is positioned at the plane of the cavity focus for HHG. The output coupler is a sapphire plate oriented at Brewster's angle with respect to the harmonic light. **IC:** input coupler, **OC:** output coupler.

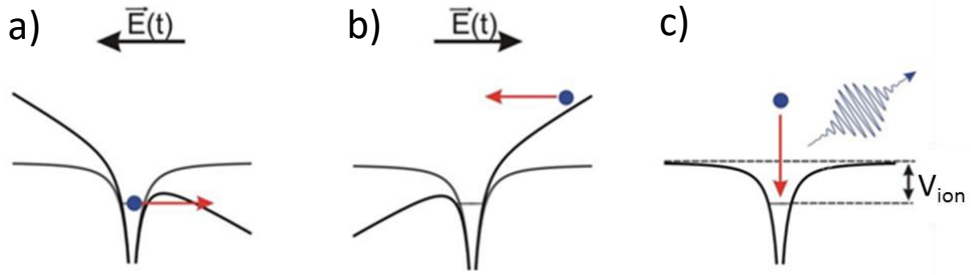

Figure 1.2. Three-step model of HHG: **(a)** tunnel ionization, **(b)** acceleration, **(c)** recombination [15].

HHG is an inefficient process owing to the low probability of electron recombination. Output harmonic powers are on the order of 10^{-6} times the power of the fundamental beam. Since the vast majority of electrons do not recombine, the generated plasma remains present in the gas jet. Depletion of the neutral gas stream reduces the number of atoms available for HHG. More importantly, the residual plasma induces a phase shift in the driving laser that leads to nonlinear effects. Nonlinearities become strong enough to impede cavity performance when the plasma-induced phase shift is approximately half the cavity linewidth [16]. This cutoff phase shift is given by π/F, where F is the cavity finesse.

The plasma-induced phase acquired during each round-trip causes a shift in the cavity resonance that leads to optical bistability (see Fig. 3.2). As the pump phase approaches the resonant detuning, the pulse achieves higher power levels. The increased pulse intensity leads to production of more plasma, which shifts the resonance further. Eventually the pulse attains its maximum enhancement, after which additional detuning causes a sharp drop in power. Scanning the pump phase in the reverse direction results in hysteresis, since significant plasma levels are not generated until the resonant detuning is applied. The hysteresis disrupts laser stabilization because servo controllers must lock to one of two possible enhancement peaks and occasionally fluctuate between the two. The lock is unstable, as too much detuning leads to a sharp drop in enhancement for which the servo cannot compensate.

Fig. 1.3 demonstrates a decrease in maximum pulse enhancement for increasing backing pressures of the gas jet. As more plasma is generated, laser pulses become more chirped due to time-dependent phase shifts (see Section 4.1). Chirp disrupts constructive interference between pulses from multiple passes, which in turn reduces power enhancement.

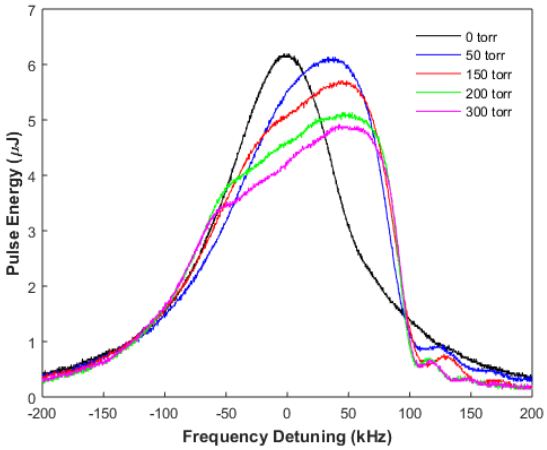

Figure 1.3. Experimental frequency scans to detect pump beam resonance for several gas jet backing pressures [17]. Raising the gas pressure leads to more plasma formation, which increases the resonance shift and decreases pulse enhancement. Hysteresis is not evident because scans were performed in only one direction.

1.4 Simulation Design

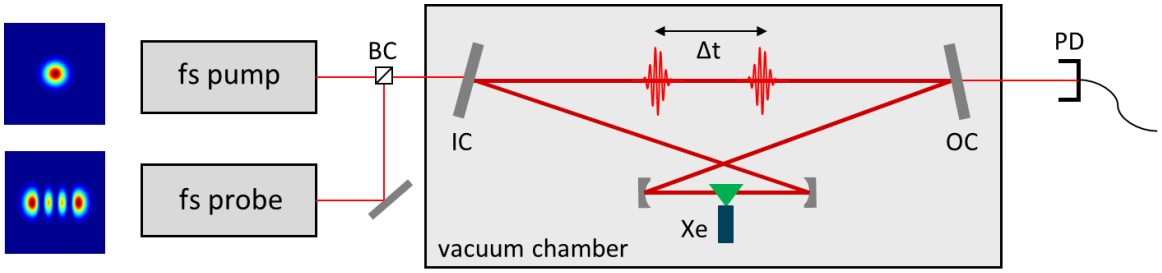

Figure 1.4. Conceptual layout for time-resolved pump-probe measurements with higher-order modes. The Gaussian pump and higher-order probe are tuned to be resonant with the cavity. The pump and probe are offset by a variable time delay Δt. A photodiode monitors the beam outputs and feeds back to servo loops for cavity stabilization (not pictured). **BC:** beam combiner, **IC:** input coupler, **OC:** output coupler, **PD:** photodiode.

The nonlinear response to residual plasma serves as the fundamental limit to our cavity performance. Through this work, we endeavor to gain intuition for plasma dynamics and the plasma-induced phase shift so that adverse nonlinear effects may be mitigated. If the issues posed by the plasma were fully rectified, we would expect a substantial improvement in HHG efficiency and cavity performance, limited by only the damage threshold of the mirrors. Our

approach is to conduct simulations of coupled laser-plasma interactions by probing with higher-order transverse modes.

The simulations presented here are based on conceptual pump-probe experiments in a femtosecond enhancement cavity (Fig. 1.4). We assume that the cavity is perfectly mode-matched. The pump beam is an intense femtosecond pulse of the fundamental Gaussian mode, which features the highest on-axis intensities for ionization of the xenon gas jet. Interaction with the plasma causes a shift in the pump resonance. The pump is dynamically tuned to maintain resonance with the cavity by compensating for the plasma-induced phase shift experienced with each pass. After enough passes, the pump and plasma reach steady-state.

The probe is a weak femtosecond pulse of a higher-order transverse mode. Higher-order modes offer unique spatial distributions and asymmetries which can probe different portions of the steady-state plasma profile. Probe resonance is also shifted by the plasma. The probe is tuned to maintain resonance while the plasma-induced phase shift is measured. Time-resolved measurements of phase shifts are achieved by introducing a variable time delay between the pump and probe. The maximum time delay is fixed by the cavity round-trip time, which we assume to be 13 ns. Alternatively, a continuous wave probe could be used for time-averaged measurements. The plasma-induced phase shift of the probe is recorded for various higher-order modes, gas jet backing pressures, and time delays. The experiment is conducted in a vacuum chamber to limit light-matter interactions exclusively to those of the lasers with the xenon jet. We neglect any phase shifts caused by thermal deformations in the cavity mirrors.

Once the above procedure is performed in the laboratory, we will fit our simulations to the experimental data. Comparing theoretical and experimental results will provide information on previously unknown plasma dynamics, such as density profiles, velocities, and decay rates.

We project that our system will enable precision measurements of plasma-induced phase shifts with microradian resolution. With this level of sensitivity, our simulations and setup could also be applied to conduct supplementary investigations. The xenon gas jet could be replaced by any transparent gas, liquid, or solid species in order to observe the resulting nonlinear phase shift. One could then obtain precision measurements of nonlinear refractive indices for a breadth of diverse materials.

1.5 Previous Experimental Results

Our group has already conducted several experiments related to this work. The relative resonance frequency shift between a Gaussian pump and a higher-order pump (HG_{30}) was measured as a function of intracavity power (Fig. 1.5). A shift in frequency corresponds to a shift in phase by the relation:

$$\Delta\nu = \frac{c/L_{tot}}{2\pi}\Delta\phi \tag{1.5.1}$$

where c is the speed of light and L_{tot} is the total cavity length. Increasing the power caused heating of the cavity mirrors. As the temperature of the curved mirrors increased, their concavity changed and introduced a relative phase between the two modes due to their different transverse profiles. Prior to ionization, the relative phase varied linearly with power. These thermal deformations were not considered in this current work. At high powers, ionization started to occur, steepening the slope of the curve relative to that of an empty cavity. This steepening reflected the relative plasma-induced phase shift between the modes. In the limit of zero intracavity power, a measurable relative phase still existed between the modes in the presence of a neutral gas jet. This shift was caused by slight variation in index of refraction over the portions of the gas jet probed by the beams. Such a shift would not occur in the simulations presented

here, as the gas jet was assumed to be uniform. Nonetheless, this phase shift demonstrates the sensitivity of cavity measurements and also provides a linear reference that could be used to reduce cavity noise.

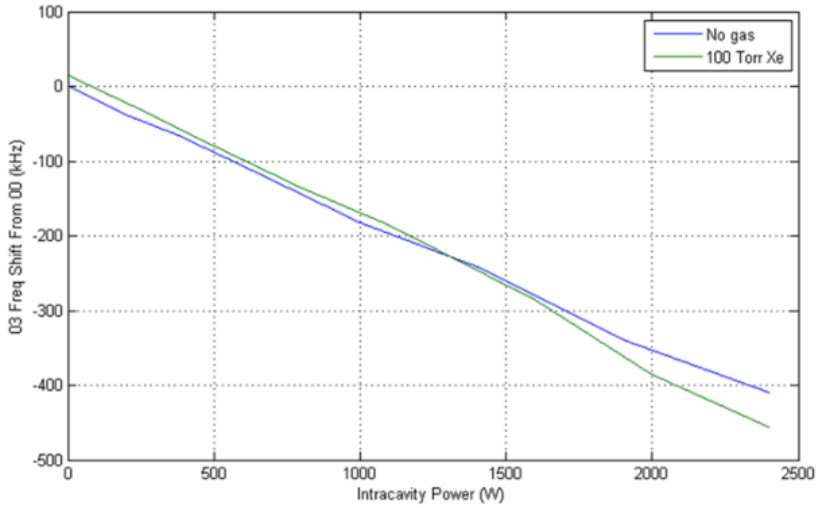

Figure 1.5. Relative resonance frequency shifts between Gaussian and HG_{30} pumps as a function of intracavity power. Measurements were obtained in an empty cavity and in the presence of a xenon gas jet. The relative frequency shift varies linearly with power due to thermal deformations in the cavity mirrors.

Time-resolved measurements of single-pass plasma generation and decay were also recorded for a variety of intracavity powers (Fig. 1.6). The setup for this inquiry was similar to that shown in Fig. 1.4, though the fundamental mode was used for both the pump and probe. Diminishing plasma densities were reflected by diminishing phase shifts experienced by the probe. As higher intracavity powers generated more plasma, the fractional decay rate due to three-body recombination increased (see Eq. (2.3.2)).

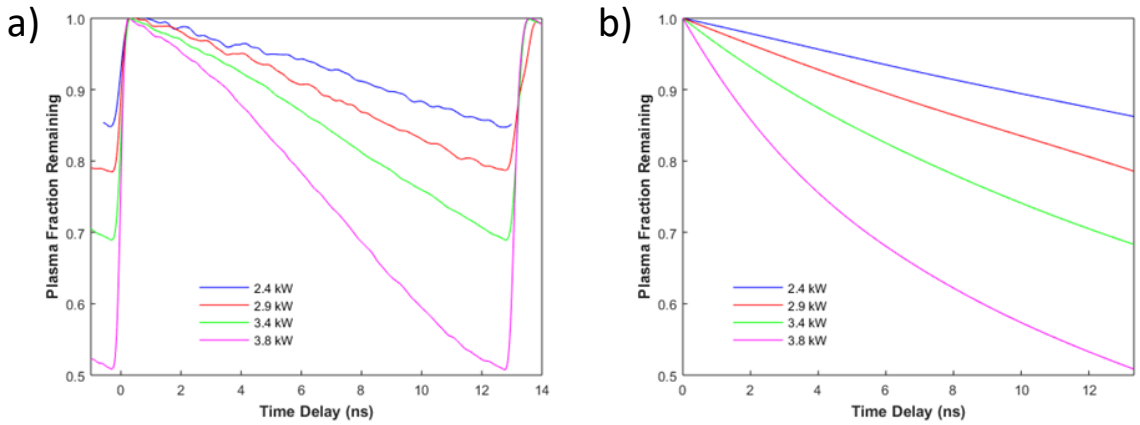

Figure 1.6. Fractional plasma decay as a function of probe delay in **(a)** experiment and **(b)** simulation. Increasing the probe time delay decreases the on-axis plasma density due to three-body recombination and gas flow. After 13 ns, the subsequent pump pulse arrives to re-ionize the gas jet. The simulation was fit to experimental results by assuming a gas velocity of 100 m/s, a neutral gas density of 1.4×10^{23} m^{-3}, and a plasma recombination coefficient of $\alpha = 1.1 \times 10^{-15}$ m^3/s.

CHAPTER 2: THEORY

2.1 Gaussian Beam Analysis

Each optical element in the enhancement cavity can be modeled as a matrix [18]. The matrices for propagation through vacuum and reflection by a curved mirror are, respectively:

$$M_{prop} = \begin{bmatrix} 1 & L \\ 0 & 1 \end{bmatrix} \tag{2.1.1}$$

$$M_{mir} = \begin{bmatrix} 1 & 0 \\ -2/R & 1 \end{bmatrix} \tag{2.1.2}$$

where L is the propagation length and R is the mirror radius of curvature. If a cavity has n optical elements, the overall ABCD matrix is calculated by multiplying the element matrices in order of interaction with the beam:

$$\begin{bmatrix} A & B \\ C & D \end{bmatrix} = M_n M_{n-1} ... M_2 M_1 \tag{2.1.3}$$

We define the complex beam parameter as:

$$Q(z) = \frac{1}{q(z)} = \frac{1}{R(z)} + \frac{2i}{k_0 w^2(z)} \tag{2.1.4}$$

where R is the radius of curvature of the beam wavefronts, k_0 is the free-space wavenumber, and w is the e^{-2} radius of the beam. After the beam propagates a distance Δz, the ABCD matrix modifies the complex beam parameter in the following manner:

$$Q(z + \Delta z) = \frac{DQ(z) + C}{BQ(z) + A} \tag{2.1.5}$$

We are concerned primarily with the plane of the intracavity focus, where the highest intensities are achieved for HHG. We define this plane as $z = 0$ and calculate the ABCD matrix for the cavity starting at this point. We are interested in maintaining a stable resonator for which the

field and the complex beam parameter are unchanged after every round-trip. To satisfy this condition, $Q(z + \Delta z) = Q(z) = Q$. Substituting into Eq. (2.1.5) and solving gives:

$$Q = \frac{D - A}{2B} + \frac{i}{|B|}\sqrt{1 - \left(\frac{A + D}{2}\right)^2} \tag{2.1.6}$$

At the intracavity focus, the beam wavefronts are planar, meaning $R(0) \to \infty$. Rearranging Eq. (2.1.4) then gives:

$$w_0 = \sqrt{\frac{2}{k_0 \mathrm{Im}[Q]}} \tag{2.1.7}$$

where $w_0 = w(0)$ is the spot size of the beam waist. For pulsed lasers, the peak power P_0 is given by:

$$P_0 = C\frac{P_{avg}}{\tau_{pulse}\upsilon_{rep}} \tag{2.1.8}$$

Where P_{avg} is the average laser power, τ_{pulse} is the pulse duration, υ_{rep} is the repetition rate, and C is a constant related to the pulse shape. For Gaussian pulses, $C \approx 0.94$, while for sech^2 pulses, $C \approx 0.88$. For simplicity, we assume square pulses ($C = 1$) for which the field does not vary over the duration of the pulse. In making this assumption, we neglect the effects of self-phase modulation caused by the time-dependent intensity of the pulse (see Section 4.1). The peak on-axis pulse intensity is given by:

$$I_0 = \frac{2P_0}{\pi w_0^2} \tag{2.1.9}$$

The electric field amplitude E and on-axis field amplitude E_0 are given by:

$$I_0 = \frac{1}{2}cn\epsilon_0 |E_0|^2 \tag{2.1.10}$$

$$I(x, y) = \frac{1}{2}cn\epsilon_0 |E(x, y)|^2 \tag{2.1.11}$$

where n is the refractive index (taken to be unity) and ϵ_0 is the permittivity of free-space.

2.2 Transverse Modes

Transverse cavity modes are given by solutions to the paraxial wave equation [18]. For this analysis, we shall describe all transverse modes using Cartesian coordinates. The amplitude and Gouy phase of the fundamental Gaussian mode are given by:

$$\varepsilon_{00}(x,y) = E_0 e^{-(x^2+y^2)/w_0^2} \tag{2.2.1}$$

$$\phi_0 = -\arg\left(\frac{1}{A+BQ}\right) \tag{2.2.2}$$

The fundamental mode serves as the intense pump pulse used to ionize the gas jet. Higher-order Hermite-Gaussian and Laguerre-Gaussian modes are used as weak probe pulses to interrogate the generated plasma.

The rectangularly symmetric Hermite-Gaussian modes (Fig. 2.1) are given by:

$$\varepsilon_{mn}(x,y) = E_0 H_m\left(\frac{x\sqrt{2}}{w_0}\right) H_n\left(\frac{y\sqrt{2}}{w_0}\right) e^{-(x^2+y^2)/w_0^2} \tag{2.2.3}$$

$$\phi_0 = -(m+n+1)\arg\left(\frac{1}{A+BQ}\right) \tag{2.2.4}$$

Where H_m and H_n represent Hermite polynomials of order m and n, respectively. We shall use the notation HG_{mn} to denote a specific Hermite-Gaussian mode. The factor $(m+n+1)$ in Eq. (2.2.4) accounts for the stronger Gouy phase shift relative to the fundamental mode. We see that for $m = n = 0$, the fundamental Gaussian mode is recovered.

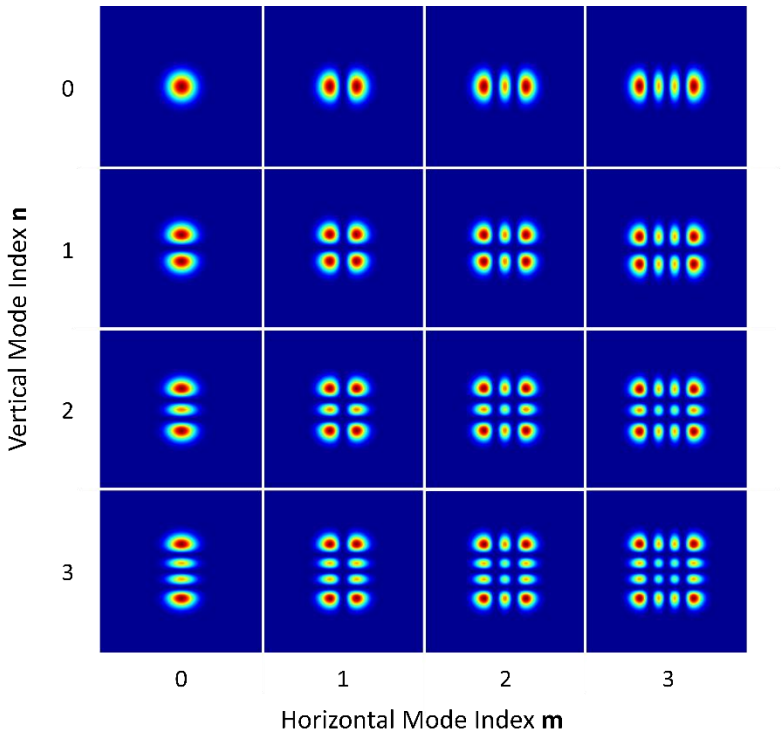

Figure 2.1. Hermite-Gaussian transverse laser mode profiles. The horizontal index **m** gives the number of horizontal field nodes, and the vertical index **n** gives the number of vertical field nodes. Modes for which both **m** and **n** are even have an on-axis peak. If either **m** or **n** is odd, the mode has an on-axis node.

The cylindrically symmetric Laguerre-Gaussian modes (Fig. 2.2) are given by:

$$\varepsilon_{p\ell}(x,y) = E_0 \left(\frac{\sqrt{2}}{w_0}\right)^{|\ell|} L_p^{|\ell|}\left[\frac{2(x^2+y^2)}{w_0^2}\right](x+iy)^{|\ell|}\, e^{-(x^2+y^2)/w_0^2} \tag{2.2.5}$$

$$\phi_0 = -(2p+|\ell|+1)\arg\left(\frac{1}{A+BQ}\right) \tag{2.2.6}$$

where $L_p^{|\ell|}$ represents an associated Laguerre polynomial. We shall use the notation $LG_{p\ell}$ to denote a specific Laguerre-Gaussian mode. The Gouy phase shift in Eq. (2.2.6) is now increased by a factor of $(2p+|\ell|+1)$ relative to the fundamental mode. Again, for $p = \ell = 0$, the fundamental Gaussian mode is recovered.

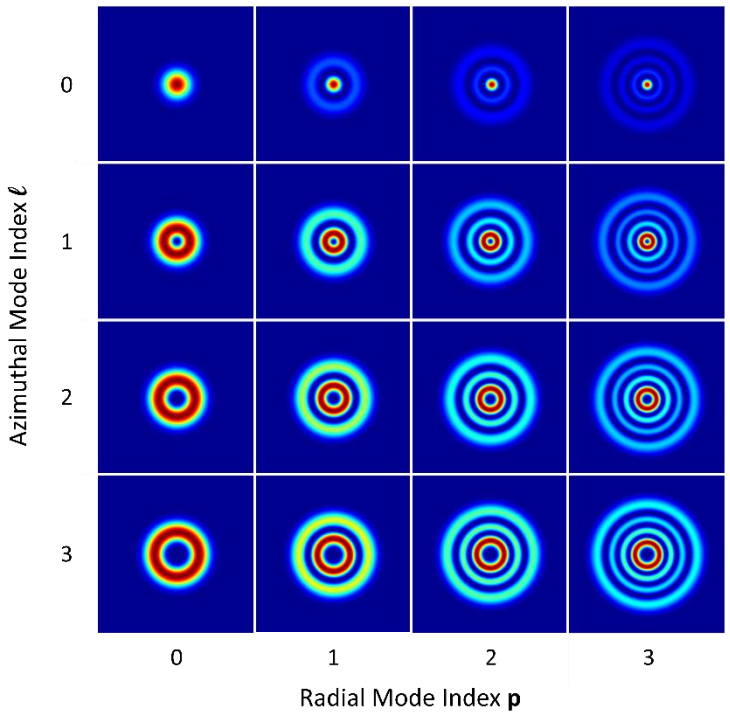

Figure 2.2. Laguerre-Gaussian transverse laser mode profiles. The radial index **p** gives the number of radial field nodes, and the azimuthal index **ℓ** describes the orbital angular momentum of the mode. Each photon has a momentum of $\ell\hbar$ about the z-axis. A nonzero azimuthal index also gives an on-axis node, with wider nodes for larger values of **ℓ**.

2.3 Plasma Generation and Decay

Our model for plasma generation is based on the Keldysh theory of strong field ionization [19]. The mechanism for ionization is specified by the Keldysh parameter, defined as:

$$\gamma = \frac{\omega}{eE}\sqrt{2m_e V_{ion}} \tag{2.3.1}$$

where ω is the driving laser frequency, E is the electric field magnitude, V_{ion} is the ionization potential of the gas, e is the electron charge, and m_e is the electron mass. Multiphoton ionization dominates for $\gamma >> 1$, while tunnel ionization dominates for $\gamma << 1$. At steady-state, our system operates in an intermediate ionization regime ($\gamma \approx 1$). One could instead consider implementing the metastable electronic state approach as an alternative ionization model [20].

Every laser pulse ionizes a certain fraction of the neutral gas jet based on the pulse intensity, ranging from no ionization at low intensities to total ionization at high intensities. The fractional ionization distribution $f(x, y)$ is determined by using the pulse intensity distribution $I(x, y)$ to index a lookup table based on Fig. 2.3.

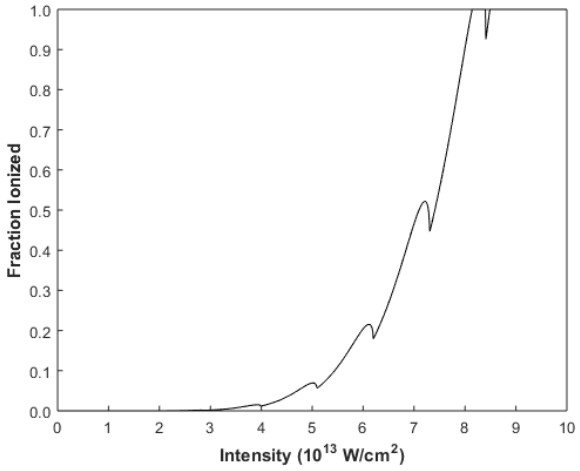

Figure 2.3. Single-pass fractional ionization of xenon for 100 fs pulses centered at 1064 nm. Analysis is based on Keldysh theory of strong field ionization.

We assume that plasma decay is dominated by three-body recombination. By this process, a free electron combines with a positive ion to form a neutral atom while another free electron stabilizes the interaction [21]. This mechanism is modeled by the equation:

$$\frac{\partial \rho(x, y)}{\partial t} = -\alpha \rho^2(x, y) \tag{2.3.2}$$

where ρ is the plasma number density and α is the recombination coefficient. Solving this differential equation gives the plasma density after decaying for a time t:

$$\rho(x, y, t) = \frac{\rho(x, y, 0)}{1 + \alpha t \rho(x, y, 0)} \tag{2.3.3}$$

For simplicity, we take the neutral gas jet to be a thin, uniform slab. Consequently, the plasma distribution does not vary as a function of propagation along the z-axis. The spatial plasma distribution after the j[th] pulse is given by:

$$\rho_j(x,y) = \eta_j(x,y)f(x,y) + \frac{\rho_{j-1}}{1+\alpha T\rho_{j-1}(x,y)} \tag{2.3.4}$$

where η is the number density of the neutral gas jet and T is the cavity round-trip time. The first term gives the plasma formed by the new pulse. The second term gives the residual plasma of the previous pulse, which has decayed due to three-body recombination. The spatial distribution of neutrals after the j[th] pulse is given by:

$$\eta_j(x,y) = \eta_{j-1}(x,y)[1-f(x,y)] + \rho_{j-1}(x,y)\left[1 - \frac{1}{1+\alpha T\rho_{j-1}(x,y)}\right] \tag{2.3.5}$$

The first term accounts for depletion of neutrals due to ionization. The second term describes neutrals that were replenished by three-body recombination. For all pulse iterations, the sum of $\rho(x,y)$ and $\eta(x,y)$ gives the finite density of the original gas jet.

2.4 Plasma-Induced Phase Shifts

Plasma locally reduces the refractive index of the gas jet according to the equation [22]:

$$n(x,y) = \sqrt{1 - \frac{\rho(x,y)}{\rho_{crit}}} \tag{2.4.1}$$

The critical plasma density of the laser ρ_{crit} is given by:

$$\rho_{crit} = \frac{\epsilon_0 m_e \omega^2}{e^2} \tag{2.4.2}$$

Above the critical plasma density, the plasma becomes opaque. For $\rho(x,y) << \rho_{crit}$ we may make the approximation:

$$n(x,y) \approx 1 - \frac{\rho(x,y)}{2\rho_{crit}} \tag{2.4.3}$$

Due to the reduction in refractive index, the pulse acquires a phase given by:

$$\Delta\phi_{plas}(x,y) = k_0 d\Delta n(x,y) = -\frac{k_0 d\rho(x,y)}{2\rho_{crit}} \tag{2.4.4}$$

where d is the thickness of the gas jet. The integrated phase shift experienced by the entire pulse upon a single pass through the plasma is calculated through the following overlap integral:

$$\Delta\phi_{pulse} = \frac{\iint \phi_{plas}(x,y)\left|\varepsilon(x,y)\right|^2 dx\, dy}{\iint \left|\varepsilon(x,y)\right|^2 dx\, dy} \tag{2.4.5}$$

where $\varepsilon(x,y)$ represents the field distribution of the transverse mode input to the cavity focus. $\Delta\phi_{pulse}$ serves as an estimate of the detuning required to keep the cavity on-resonance by compensating for the nonlinear phase shift of the plasma.

Intense pulses also experience self-focusing caused by the nonlinear Kerr effect. The resulting phase shift for the pump pulse is:

$$\Delta\phi_{Kerr}(x,y) = k_0 d n_2 I(x,y) \tag{2.4.6}$$

where n_2 is the nonlinear index of the gas. This phase shift opposes the plasma-induced phase shift ($\Delta\phi_{Kerr}$ is positive, $\Delta\phi_{plas}$ is negative). For our assumed pulse intensities, the nonlinear interactions of the pulse are dominated by the effects of the plasma ($\Delta\phi_{Kerr} << \Delta\phi_{plas}$). The Kerr effect was neglected in probe pulses, which were assumed to be weak. The total phase of the pulse is given by:

$$\phi_{tot}(x,y) = \phi_0 + \Delta\phi_{plas}(x,y) + \Delta\phi_{Kerr}(x,y) \tag{2.4.7}$$

2.5 Field Propagation

Propagation of the electric field is described by the generalized Huygens integral in two dimensions:

$$E_j{}'(x',y') = \sqrt{\frac{k_0}{i2\pi B}} \iint_{-\infty}^{\infty} dx\, dy\, \exp\left\{\frac{ik_0}{2B}\Big[Ax^2 - 2xx' + D(x')^2\Big]\right\} \times \exp\left\{\frac{ik_0}{2B}\Big[Ay^2 - 2yy' + D(y')^2\Big]\right\} E_{j-1}(x,y) e^{i\phi_{tot}(x,y)} \tag{2.5.1}$$

where the field of the previous pulse $E_{j-1}(x,y)$ is propagated through the cavity to give $E_j{}'(x',y')$. We employ the proper ABCD matrix elements for a cavity round-trip. The exponential term containing D may be separated from the integral as follows:

$$E_j{}'(x',y') = \exp\left\{\frac{ik_0}{2B}(D-1)\Big[(x')^2+(y')^2\Big]\right\}\sqrt{\frac{k_0}{i2\pi B}} \iint_{-\infty}^{\infty} dx\, dy\, \exp\left\{\frac{ik_0}{2B}\Big[x^2 - 2xx' + (x')^2\Big]\right\} \times \exp\left\{\tfrac{ik_0}{2B}\Big[y^2 - 2yy' + (y')^2\Big]\right\} \exp\left\{\frac{ik_0}{2B}(A-1)(x^2+y^2)\right\} E_{j-1}(x,y) e^{i\phi_{tot}(x,y)} \tag{2.5.2}$$

We then define:

$$G_1 = \exp\left\{\frac{ik_0}{2B}(A-1)(x^2+y^2)\right\} \tag{2.5.3}$$

$$G_2 = \exp\left\{\frac{ik_0}{2B}(D-1)\Big[(x')^2 + (y')^2\Big]\right\} \tag{2.5.4}$$

The remaining exponential describes propagation over free space. Using the definition of a Fourier transform $\mathcal{F}$, we have:

$$E_j{}'(x',y') = G_2\sqrt{\frac{k_0}{i2\pi B}} \cdot \mathcal{F}^{-1}\Big\{K \cdot \mathcal{F}\Big[G_1 E_{j-1}(x,y) e^{i\phi_{tot}(x,y)}\Big]\Big\} \tag{2.5.5}$$

where the paraxial propagator K is given by:

$$K = \exp\left\{-\frac{iB}{2k_0}(k_x^2 + k_y^2)\right\} \tag{2.5.6}$$

The electric field of the j[th] pulse is then:

$$E_j(x,y) = rE_j{}'(x',y') + \tau\varepsilon(x,y) \tag{2.5.7}$$

The reflection coefficient r and transmission coefficient τ are defined as:

$$r = \sqrt{R_{IC}R_{tot}} \tag{2.5.8}$$

$$\tau = i\sqrt{1-R_{IC}} \tag{2.5.9}$$

where R_{IC} is the reflectance of the input coupler and $1-R_{tot}$ represents all other cavity losses.

The maximum theoretical cavity enhancement is:

$$\frac{P_{max}}{P_0} = \frac{4(1-R_{IC})}{[1-(R_{IC}R_{tot})]^2} \tag{2.5.10}$$

Based on the assumed cavity losses, a maximum theoretical enhancement of 179 was expected.

CHAPTER 3: RESULTS

3.1 Stationary Gas Jet Phase Shifts

Through iterative cycles of propagation with the Gaussian pump, the field and plasma profiles reached steady-state (Fig. 3.1). The steady-state field enhancement was recorded for a range of phase detunings applied to the field (Fig. 3.2). When scanning across the phase, the steady-state field and plasma for the previous detuning were used to initialize the field and plasma for the new detuning.

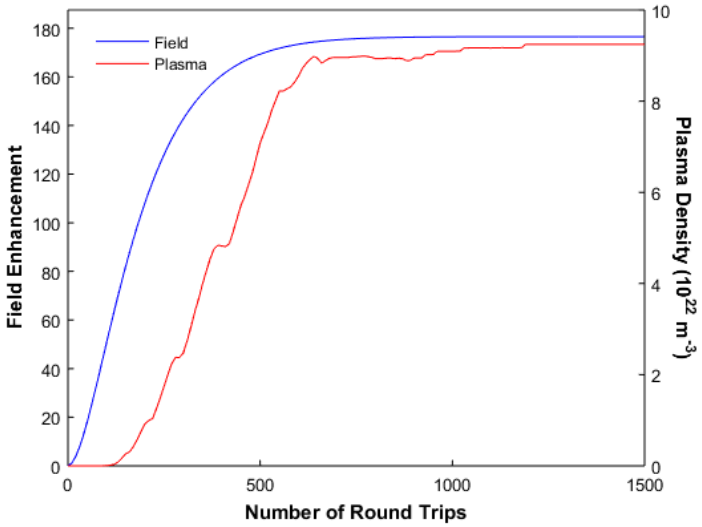

Figure 3.1. Buildup of the pump field and plasma profile to steady-state. For the resonant detuning of 5.1 mrad, the pump nearly reaches its maximum theoretical enhancement of 179.

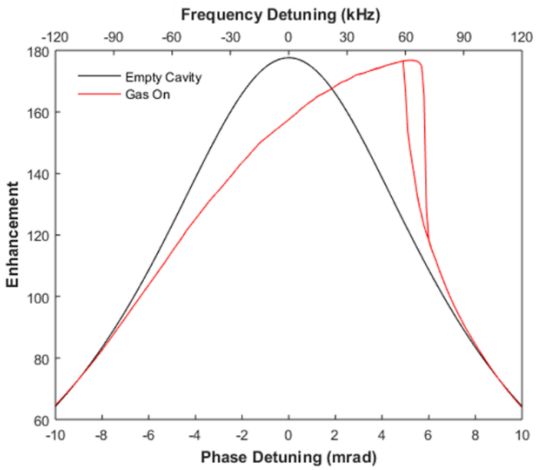

Figure 3.2. Phase scans to detect pump beam resonance with and without plasma interactions. For an empty cavity, scanning across the phase yields a Lorentzian lineshape for power enhancement with a full width at half maximum of 180 kHz. Maximum buildup is achieved for zero detuning. In the presence of plasma, the resonance is shifted, and hysteresis in the cavity enhancement indicates optical bistability.

With the gas jet on, the pump field and plasma were built up to steady-state using the resonant phase detuning. A selected higher-order probe beam was then used to interrogate the plasma (Fig. 3.3). The probe beam was scanned across a range of phase detunings to observe the plasma-induced shift in the cavity resonance (Fig. 3.4). In the presence of plasma, different modes experienced different phase shifts based on the spatial overlap with the plasma profile.

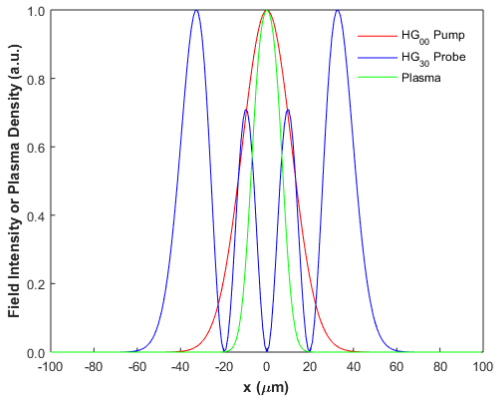

Figure 3.3. Normalized steady-state profiles for the Gaussian pump, a HG_{30} probe, and the intracavity plasma. The Gaussian distribution of the plasma is more confined than that of the pump. Phase shifts experienced by the probe are determined by the level of overlap with the plasma. In this example, the phase shift of HG_{30} is 0.93 mrad.

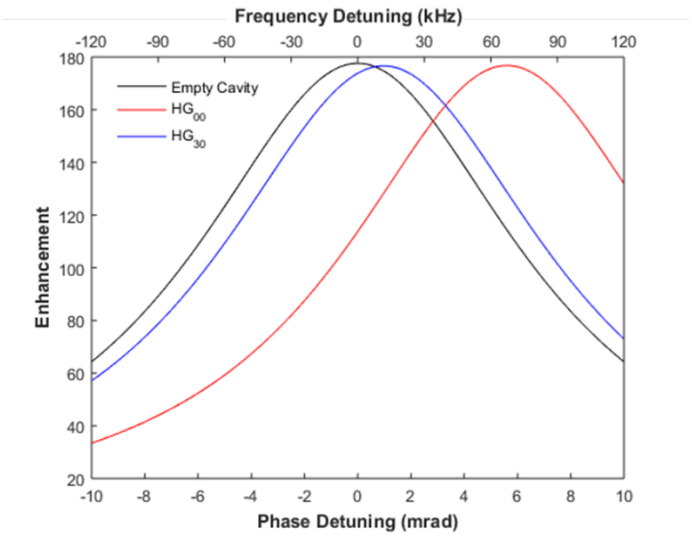

Figure 3.4. Phase scans to detect probe beam resonance with and without plasma interactions. For an empty cavity, all modes exhibit the same Lorentzian lineshape for power enhancement, with maximum buildup achieved at zero detuning. In the presence of plasma, HG_{00} experiences a stronger resonance shift than HG_{30} due to greater spatial overlap with the plasma profile. The weak probe beams have no influence on the plasma profile, precluding optical bistability.

Measurements of the shift in the cavity resonance were compared with the single-pass phase shifts predicted by Eq. (2.4.5) (Table 3.1). The predicted single-pass shift deviated from the actual cavity shift by a maximum of approximately 5%. We conclude that applying Eq. (2.4.5) is a sufficiently accurate alternative to scanning for resonance across phase detunings. This approximation enabled substantially faster simulations, as the pump and probe beams could be kept on-resonance dynamically by compensating for the estimated single-pass phase shift during each round-trip.

Table 3.1. Comparison of plasma-induced resonance shifts with single-pass phase shifts predicted by Eq. (2.4.5) for higher-order probe beams.

Mode	$\Delta\phi_{res}$ (mrad)	$\Delta\phi_{pulse}$ (mrad)	Error
HG_{10}	0.904	0.873	3.43%
HG_{20}	2.072	1.969	4.97%
HG_{30}	0.952	0.913	4.10%
HG_{11}	0.159	0.156	1.89%

The single-pass phase shift was estimated for a variety of transverse modes used as a probe (Table 3.2). Modes with an on-axis node interacted with significantly less plasma and experienced smaller phase shifts. Since the gas jet was assumed to be uniform and stationary, vertical HG modes (e.g. HG_{01}) were effectively equivalent to their horizontal counterparts. The phase shift of the intense Gaussian pump was smaller than that of a weak Gaussian probe due to an opposing phase shift caused by the nonlinear Kerr effect. Enhancement was lowest for HG_{20} because of distortion caused by focusing effects (see Section 3.4).

Table 3.2. Single-pass phase shift, corresponding frequency shift, and maximum enhancement for higher-order probe beams.

Mode	$\Delta\phi_{pulse}$ (mrad)	$\Delta\nu_{pulse}$ (kHz)	Enh
Pump	4.9	58.5	176.53
HG_{00}/LG_{00}	5.3	63.3	176.45
HG_{10}	0.88	10.5	177.54
HG_{20}	2.0	23.9	166.28
HG_{30}	0.93	11.1	176.64
HG_{01}	0.88	10.5	177.54
HG_{02}	2.0	23.9	166.28
HG_{03}	0.93	11.1	176.64
HG_{11}	0.16	1.91	177.62
HG_{22}	0.75	8.95	172.71
LG_{10}	3.8	45.4	176.93
LG_{20}	3.0	35.8	176.51
LG_{30}	2.5	29.8	176.88
LG_{01}	0.88	10.5	177.54
LG_{02}	0.16	1.91	177.62
LG_{03}	0.03	0.358	177.62
LG_{11}	1.2	14.3	177.51
LG_{22}	0.45	5.37	177.60

3.2 Gas Jet Velocity and Plasma Recombination

A more realistic model of plasma generation accounted for flow of the gas jet. The plasma and neutral atoms were assumed to move with a uniform velocity along a single direction transverse to the beam propagation. Divergence of the gas jet was neglected. Incorporating flow caused the residual plasma to move off-axis while decaying. For low velocities, the result was a smearing of the previously Gaussian plasma profile (Fig. 3.5a-b). At high velocities, the Gaussian plasma distributions produced by each pulse were displaced far enough during a round-trip to be resolvable. This produced a train of diminishing, evenly spaced Gaussian density profiles (Fig. 3.5c). Increasing the velocity also decreased the buildup of on-axis plasma.

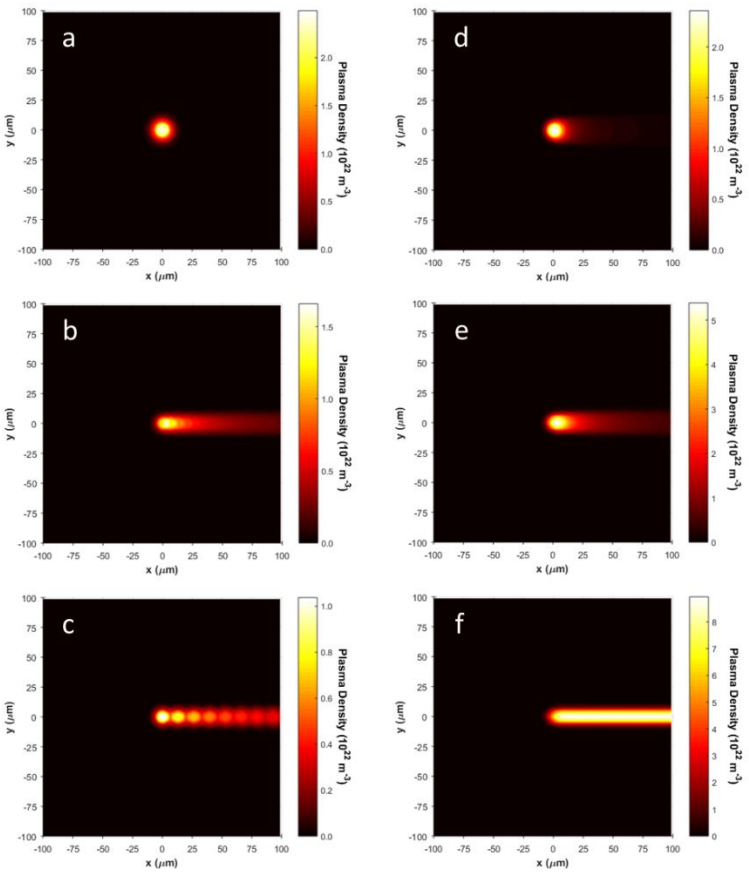

Figure 3.5. Steady-state plasma profiles resulting from a flowing gas jet. The profiles on the left represent a fixed recombination coefficient of $\alpha = 2.0 \times 10^{-15}$ m^3/s and gas velocities of **(a)** 0 m/s, **(b)** 500 m/s, and **(c)** 1000 m/s. The profiles on the right represent a fixed gas velocity of 100 m/s and assumed recombination coefficients of **(d)** $\alpha = 2.0 \times 10^{-15}$ m^3/s, **(e)** $\alpha = 0.2 \times 10^{-15}$ m^3/s, and **(f)** $\alpha = 0$ m^3/s.

Steady-state plasma profiles were influenced by recombination rates as well. Weaker recombination increased plasma buildup and enabled plasma to be carried farther off-axis (Fig. 3.5d-f). The highest plasma-induced phase shifts in the pump thus occurred for low velocities and weak recombination rates (Fig. 3.6).

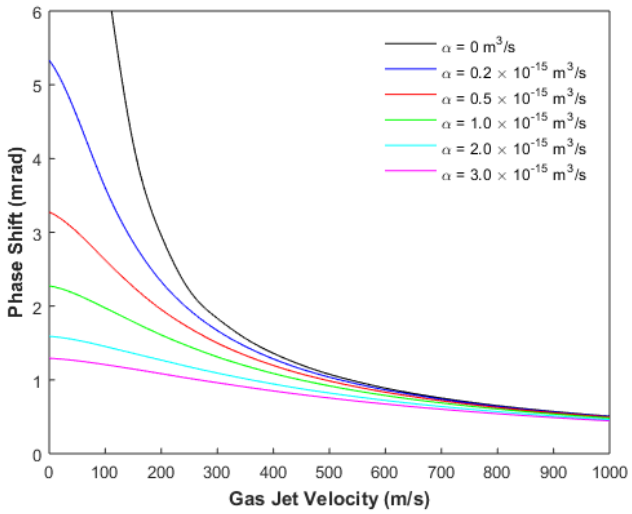

Figure 3.6. Plasma-induced phase shifts in the Gaussian pump as a function of gas velocity for several assumed plasma recombination coefficients. Higher velocities and recombination rates decrease the on-axis plasma buildup, reducing the phase shift experienced by the pump. Probing the plasma with any mode featuring an on-axis peak would give similar results.

The off-axis smearing of the plasma profile uniquely affects the phase shift experienced by probes having a central node. Higher velocities push residual plasma farther off-axis to overlap more with the peaks of the mode. However, higher velocities also decrease the buildup of plasma as more is carried away. Balancing these two effects, these modes experience the largest phase shift for a single optimal velocity. The optimum velocity is characteristic of a given recombination rate (Fig. 3.7). Therefore, if one could vary the pressure of the gas jet with knowledge of its velocity to find the maximum phase shift, one could experimentally determine the recombination coefficient of the plasma. Alternatively, if the recombination rate were known, one could ascertain which gas pressure corresponds to the optimum velocity. Increasing the

recombination rate or the time delay between pump and probe monotonically decreases the phase shift for a given velocity. Repeating these measurements for a delay between the pump and probe would lower the phase shifts of a given recombination curve and shift the peak to lower velocities. Similar trends would also be evident for a continuous wave pump-probe setup, which would give smoother steady-state plasma profiles that do not depend on probe delay times.

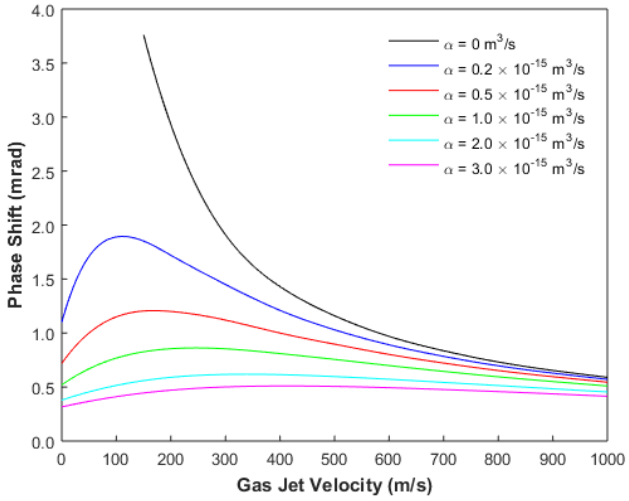

Figure 3.7. Plasma-induced phase shifts in a HG_{30} probe as a function of gas velocity for several assumed plasma recombination coefficients. For each recombination coefficient, a maximum phase shift is produced for a single, optimum velocity. The pump and probe were assumed to be coincident. Probing the plasma with any mode featuring an on-axis node would give similar results.

3.3 Probe Beam Distortion

Any Laguerre-Gaussian mode can be expressed as a linear combination of Hermite-Gaussian modes and vice-versa. Mathematically, both types of modes together form a complete set. Several mode superpositions are illustrated in Fig. 3.8.

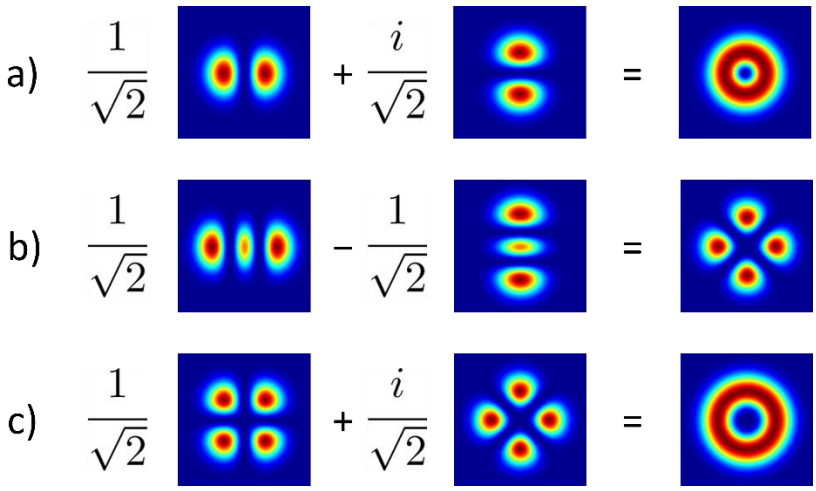

Figure 3.8. Linear superpositions of Hermite-Gaussian modes [23]. **(a)** HG_{10} and HG_{01} combine to give LG_{01}. **(b)** HG_{20} and HG_{02} combine to give a $\pi/4$ rotation of HG_{11}. **(c)** HG_{11} and a $\pi/4$ rotation of HG_{11} combine to give LG_{02}.

In the absence of gas flow, the plasma distribution has a symmetric Gaussian profile. As shown in Table 3.2, modes that are equivalent save for a rotation (e.g. HG_{10} and HG_{01}) experience identical plasma-induced phase shifts. When accounting for gas jet motion, plasma is pushed along the direction of flow (Fig. 3.5). For horizontal flow, horizontal modes overlap with plasma more than vertical modes and acquire a stronger phase shift. When LG_{01} is used as a probe, the constituent HG_{10} and HG_{01} modes acquire a phase shift relative to one another. Since the ideal LG_{01} mode requires a $\pi/2$ relative phase between the constituent modes (Fig. 3.9), the relative phase shift due to the plasma leads to beam distortion (Fig. 3.10). The same principle applies to LG_{02}, which is a superposition of HG_{11}, HG_{20}, and HG_{02}.

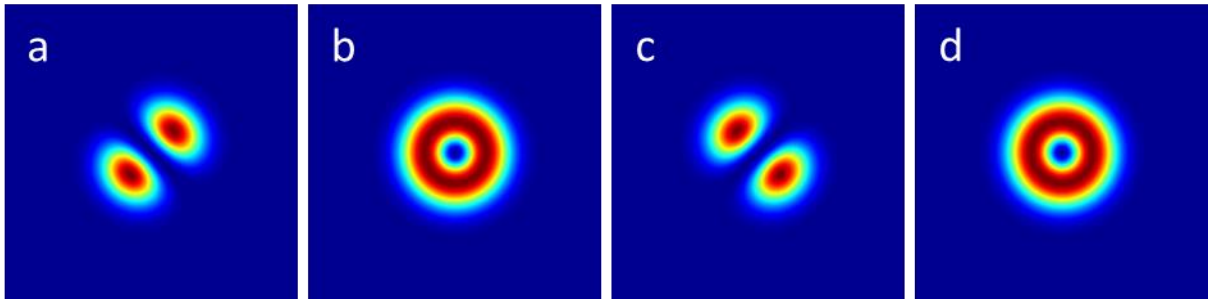

Figure 3.9. Superpositions of HG_{10} and HG_{01} with a relative phase of **(a)** 0, **(b)** $\pi/2$, **(c)** π, and **(d)** $3\pi/2$. HG_{10} has the same spatial profile as **(a)** and **(c)**, save for a $\pi/4$ rotation about the propagation axis. LG_{01} is produced in **(b)** and **(d)**. Plasma-induced relative phase shifts lead to steady-state beam profiles between **(b)** and **(c)** when using LG_{01} as a probe.

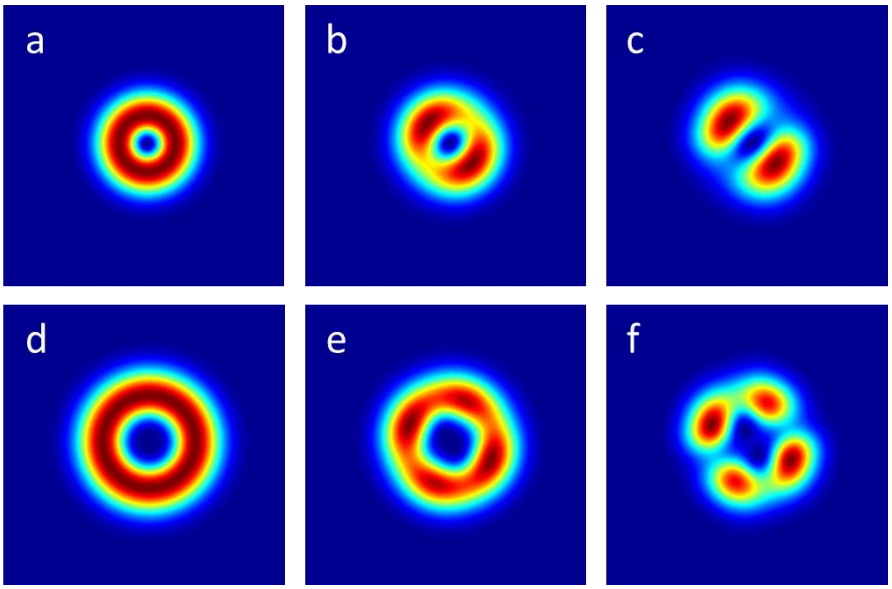

Figure 3.10. Distorted steady-state beam profiles for LG_{01} **(a-c)** and LG_{02} **(d-f)**. **(a)** represents a stationary gas jet with $\alpha = 2.0 \times 10^{-15}$ m^3/s (plasma in Fig. 3.5a), **(b)** represents a 100 m/s gas jet with $\alpha = 0.2 \times 10^{-15}$ m^3/s (plasma in Fig. 3.5e), and **(c)** represents a 100 m/s gas jet with no recombination (plasma in Fig. 3.5f). The same applies for **(d)**, **(e)**, and **(f)**, respectively. As relative phase shifts increase, the Laguerre-Gaussian beams more closely resemble their Hermite-Gaussian constituents. The constituents of LG_{01} are $\pi/2$ rotations of one another, so the distorted beam is rotated by $\pi/4$. The constituents of LG_{02} are $\pi/4$ rotations of one another, so the distorted beam is rotated by $\pi/8$.

In order to quantify the magnitude of beam distortion, we define the "distortion fraction" as $(I_{peak} - I_{valley})/I_{peak}$ (Fig. 3.11). The distortion fraction in a LG_{01} probe was measured for a series of recombination coefficients and gas jet velocities (Fig. 3.12a). Using the same gas jet

conditions, HG_{10} and HG_{01} were also used as probes to determine their relative phase shifts (Fig. 3.12b). The results are very similar to those presented in Fig. 3.7, which was to be expected as both LG_{01} and HG_{30} have an on-axis node. There is again an optimum velocity for which the plasma has maximum overlap with the HG_{10} constituent, giving rise to the greatest phase shift relative to HG_{01}. Scanning over velocities to find the maximum distortion in LG_{01} thus represents an alternative method for determining the plasma recombination coefficient. Unlike the absolute phase shifts presented in Fig. 3.7, the relative phase shift between HG_{10} and HG_{01} falls to zero for a stationary gas jet and is more sharply peaked at the optimum velocity. Provided that detectors could precisely resolve beam distortion, probing with LG_{01} is in principle the more sensitive method.

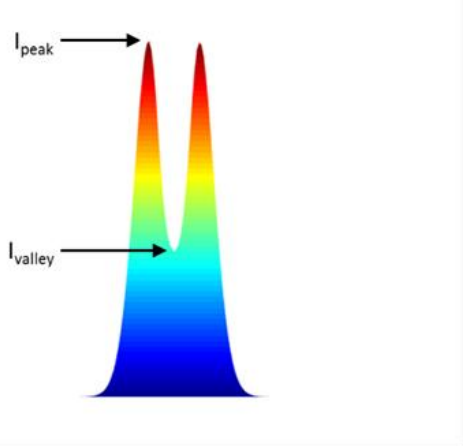

Figure 3.11. Profile of a distorted LG_{01} beam. I_{peak} represents the maximum intensity of the beam. I_{valley} represents a saddle point in the beam intensity.

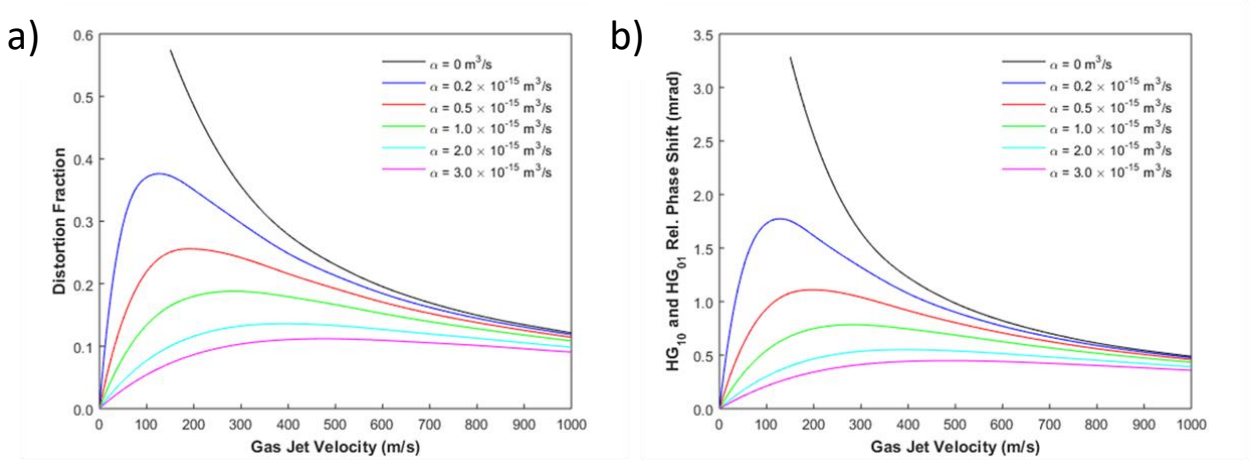

Figure 3.12. (a) Distortion in a LG_{01} probe and **(b)** relative plasma-induced phase shifts between HG_{10} and HG_{01} probes as a function of gas velocity for several assumed plasma recombination coefficients. The results demonstrate that distortion in LG_{01} is a direct consequence of relative phase shifts between the constituent HG_{10} and HG_{01} modes. The single-pass relative phase shifts in **(b)** are orders of magnitude lower than the phases required to produce the steady-state distortions observed in **(a)** and Fig. 3.10. The steady-state beam represents constructive interference of pulses from many round-trips, so the single-pass phase shift is magnified accordingly.

3.4 Beam Focusing

For sufficiently high pump powers, plasma-induced phase shifts can lead to distortion of the beam. The plasma phase profile is strongest on-axis, which has the effect of a diverging lens. Counterintuitively, we have found that the diverging effect of the plasma serves to *focus* the beam at the gas jet (Fig. 3.13). Our assumed cavity design responds favorably to the presence of a slightly negative lens at the intracavity focus. Positive feedback occurs because the increased intensity of the pump achieves more ionization, causing a stronger focusing effect. Once enough plasma is present for the focusing to be significant, a small increase in power leads to total ionization of all the atoms on-axis. Depletion of neutrals in the gas jet curtails the runaway self-focusing since no additional plasma can be generated on-axis, though the plasma profile may still grow spatially. Beam distortion is most apparent when probing with HG_{20} (Fig. 3.14). This mode

is maximally sensitive to focusing because it is circularly asymmetric and the on-axis peak is substantially weaker than the adjacent peaks.

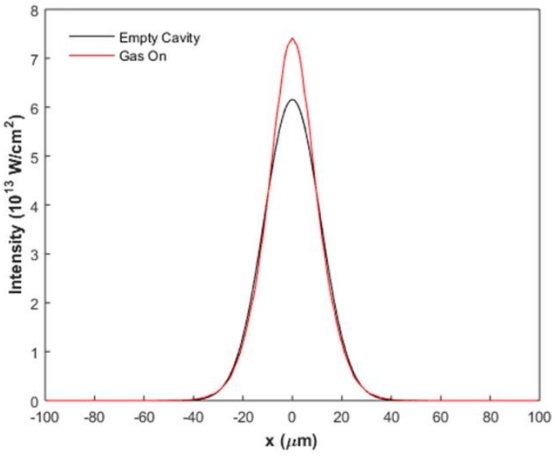

Figure 3.13. Steady-state intensity profile of the pump beam at the intracavity focus. Higher on-axis intensities are achieved when the pulse interacts with the plasma than when the cavity is empty.

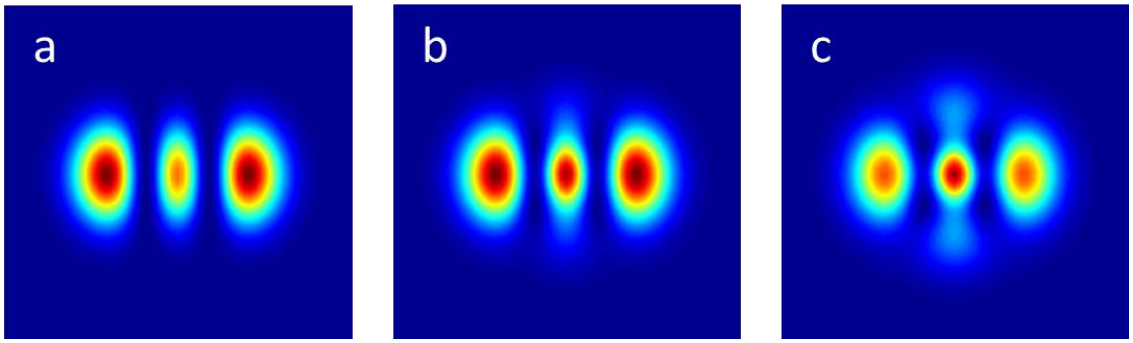

Figure 3.14. Distorted steady-state beam profiles for HG_{20} for pump powers of **(a)** 19 W, **(b)** 21 W, and **(c)** 22 W. At low pump powers **(a)**, the generated plasma density is too low to induce self-focusing. The steady-state probe closely resembles the input HG_{20} mode. When the pump power is high enough to generate sufficient plasma for focusing **(b)**, the steady-state probe becomes more intense on-axis. At slightly higher pump powers **(c)**, the gas jet is fully ionized on-axis, causing significant distortion of the probe. Further increases in pump power have little influence on the beam profile.

Though plasma interactions appear to be beneficial based on these results, the overall effect of intracavity plasma is detrimental. This model neglects self-phase modulation induced by the plasma, which decreases pulse enhancement. The decrease in pulse intensity due to chirp

would compete with the increase in intensity due to focusing, making runaway ionization unlikely. This model is therefore most valid for pump powers low enough to avoid significant beam focusing.

All results presented in Section 3.1 represent an input pump power of 21 W, for which the beam was subjected to plasma focusing. Consequently, simulated plasma densities and phase shifts were likely higher than one would observe in experiment, where pulse chirp would oppose focusing. The results in Sections 3.2 and 3.3 are more realistic, as an input pump power of 17 W was assumed and minimal focusing took place.

CHAPTER 4: FUTURE WORK

4.1 Self-Phase Modulation

Our model assumes that the laser pulses have a square temporal profile. By neglecting the time-dependent intensity of the pulses, we neglect the occurrence of time-dependent phase shifts and self-phase modulation. Despite this assumption, experiments have confirmed that plasma-induced self-phase modulation impedes cavity enhancement by introducing pulse chirp [17]. This serves as the fundamental limit to HHG efficiency in our cavity.

Accounting for chirp would decrease constructive interference between pulses from multiple passes and decrease steady-state power enhancement. Lower pulse intensities would reduce ionization as well as all expected phase shifts. Plasma-induced chirp serves as negative feedback for ionization that would compete with the positive feedback caused by the focusing effects discussed in Section 3.4. The Kerr effect is only significant for high intensities, so we may always neglect self-phase modulation in the weak probe pulses.

To expand our model to incorporate the effects of self-phase modulation, we modify Eq. (2.4.6) to give the instantaneous Kerr phase shift:

$$\Delta\phi_{Kerr}(x,y,t) = k_0 dn_2 I(x,y,t) \tag{4.1.1}$$

where we have accounted for the time-dependent intensity of the pulse. We assume that the pulse has a Gaussian temporal profile:

$$I(x,y,t) = I(x,y)e^{-8t^2/\tau_{pulse}^2} \tag{4.1.2}$$

We must now set $C \approx 0.94$ in Eq. (2.1.8) to reflect a Gaussian pulse shape. For linear pulse propagation, we convert the temporal profile into the frequency domain through an appropriate Fourier transform. We then apply a transfer function to model a round-trip through the cavity.

The pulse is then converted back to the time domain for simulations of time-dependent phase shifts caused by the plasma. This procedure must be executed in addition to the spatial propagation outlined in Section 2.5. By adding a third pulse dimension, we drastically increase the computation time of the simulations.

4.2 Gas Jet Profiles

Further work could be performed to refine our simulations of the xenon gas jet. Our current model assumes that the gas is a uniform slab of a fixed thickness that flows with a single velocity along one direction. In reality, the density, thickness, and velocity of the gas jet are all functions of position. An accurate representation of the gas jet calls for rigorous simulations involving computational fluid dynamics. Sample results of such simulations are presented in Fig. 4.1.

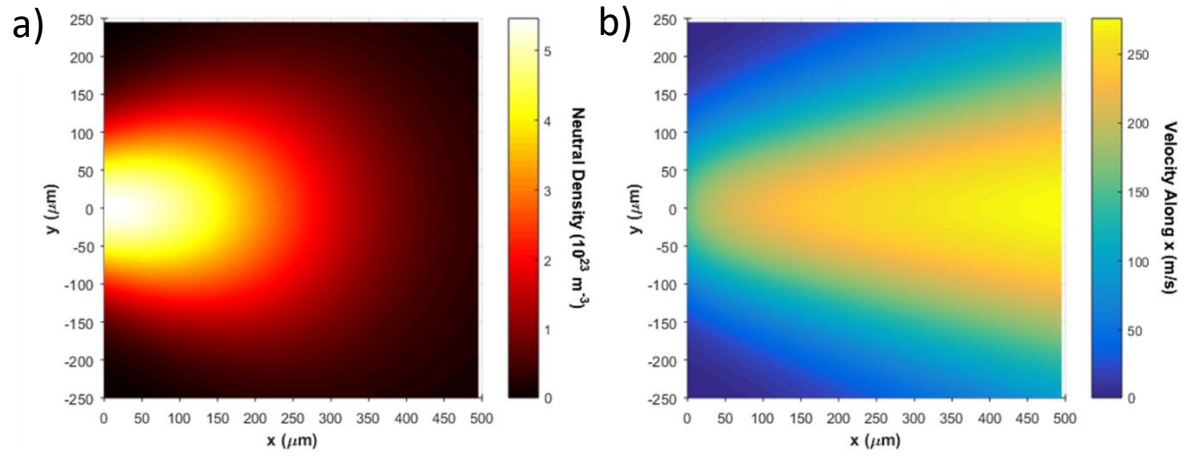

Figure 4.1. Example simulations of xenon jet **(a)** density and **(b)** velocity along the nozzle axis. The plots are based loosely on fits of data presented in [21]. The plane is transverse to the direction of laser propagation. The gas exits a nozzle of width 300 μm located at x = 0. Flow is directed along x. Density falls off like a Gaussian with distance from the nozzle and with distance from the center of the jet. Velocity along the gas propagation direction increases logarithmically with distance from the nozzle and falls off like a Gaussian with distance from the center of the jet. The laser should be located near the nozzle to utilize the high density of neutrals, but not so close that the beam is clipped.

Deviations in the density or thickness of the gas over the spot size of the beam (≈ 20 μm) are unlikely to influence results noticeably. However, variation in the direction and velocity of gas flow would affect the steady-state plasma profiles shown in Fig. 3.5. The divergence of the gas jet would spread out the plasma over a larger area, which could increase the overlap with certain modes and raise the phase shift. Probing with higher-order modes could then become even more useful for studying the divergence and local velocities of the gas jet. One could also determine the optimal beam location that maximizes ionization while minimizing the residual plasma. Nonetheless, the general trends displayed in Fig. 3.7 and Fig. 3.12 are unlikely to change with added complexity of the gas jet. Our current model is sufficient for obtaining an estimate of gas velocity, plasma recombination, and plasma-induced phase shifts.

4.3 Comparison with Experimental Results

The results presented here are not intended to formulate new analytical models of plasma dynamics. Absolute plasma-induced phase shifts are a function of dozens of variables, and each of those variables contributes uncertainty to simulation results. Minor alterations to the design of the gas jet nozzle can radically affect gas flow [21], which in turn changes the expected phase shifts. Expanding the complexity of this model in a manner that presumes experimental control over all system parameters would serve only to convolute the results and to obscure physically significant trends. Rather, the simulations are best used for constructing fits of laboratory results in order to gain intuition for the dependence of cavity performance on select system parameters. This work will attain its full utility when experiments can be conducted and analyzed in parallel with the simulations. In anticipation of such investigations, we have proposed methods for estimating spatial plasma profiles, gas jet velocities, and the plasma recombination coefficient.

Our approach is based on probing plasma-induced phase shifts with higher-order transverse modes. Elucidating intracavity plasma dynamics will reveal the most effective techniques for mitigating residual plasma and improving intracavity HHG efficiency.

REFERENCES

[1] A. Baltuška, M. Uiberacker, E. Goulielmakis, R. Kienberger, V. S. Yakovlev, T. Udem, T. W. Hänsch, and F. Krausz, *IEEE Journal of Selected Topics in Quantum Electronics* **9**, 972 (2003).

[2] N. Oliveira, M. Roudjane, D. Joyeux, D. Phalippou, J. C. Rodier, and L. Nahon, *Nature Photonics* **5**, 149 (2011).

[3] J. Lee, D. Carlson, and R. J. Jones, *Opt. Express* **19**, 23315 (2011).

[4] A. Cingöz, D. C. Yost, T. K. Allison, A. Ruehl, M. E. Fermann, I. Hartl, and J. Ye, *Nature* **482**, 68 (2012).

[5] D. R. Carlson, T. H. Wu, and R. J. Jones, *CLEO: Science and Innovations*, 2267 (2015).

[6] I. Coddington, W. C. Swann, and N. R. Newbury, *Phys. Rev. Lett.* **100**, 013902 (2008).

[7] J. Liu, E. J. Salumbides, U. Hollenstein, J. C. J. Koelemeij, K. S. E. Eikema, W. Ubachs, and F. Merkt, *J. Chem. Phys.* **130**, 174306 (2009).

[8] D. Sprecher, C. Jungen, W. Ubachs, and F. Merkt, *Faraday Discuss.* **150**, 51 (2011).

[9] W. H. Wing, G. A. Ruff, W. E. Lamb, and J. J. Spezeski, *Phys. Rev. Lett.* **36**, 1488 (1976).

[10] E. Reinhold, R. Buning, U. Hollenstein, A. Ivanchik, P. Petitjean, and W. Ubachs, *Phys. Rev. Lett.* **96**, 151101 (2006).

[11] B. R. Beck, J. A. Becker, P. Beiersdorfer, G. V. Brown, K. J. Moody, J. B. Wilhelmy, F. S. Porter, C. A. Kilbourne, and R. L. Kelley, *Phys. Rev. Lett.* **98**, 142501 (2007).

[12] W. G. Rellergert, D. DeMille, R. R. Greco, M. P. Hehlen, J. R. Torgerson, and E. R. Hudson, *Phys. Rev. Lett.* **104**, 200802 (2010).

[13] M. Lewenstein, P. Balcou, M. Y. Ivanov, A. L'Huillier, and P. B. Corkum. *Phys. Rev. Lett.* **49,** 2117 (1994).

[14] P. B. Corkum, *Phys. Rev. Lett.* **71**, 1994 (1993).

[15] C. Winter, "High-order Harmonic Generation," *WWU Münster,* http://www.unimuenster.de/Physik.PI/Zacharias/en/research/hh/hhg.html.

[16] K. D. Moll, R. J. Jones, and J. Ye, *Opt. Express* **13**, 1672 (2005).

[17] D. R. Carlson, J. Lee, J. Mongelli, E. M. Wright, and R. J. Jones, *Opt. Lett.* **36**, 2991 (2011).

[18] P. W. Milonni and J. H. Eberly, *Laser Physics*, Wiley (2010).

[19] L. V. Keldysh, *Sov. Phys. JETP* **20**, 1307 (1964).

[20] A. Bahl, E. M. Wright, and M. Kolesik, *Phys. Rev. Lett.* **94**, 023850 (2016).

[21] T. J. Hammond, *Intracavity Generation of High Order Harmonics,* Diss, The University of British Columbia (2011).

[22] P. Gibbon, *Short Pulse Laser Interactions with Matter,* Imperial College Press (2005).

[23] M. W. Beijersbergen, L. Allen, H. E. L. O. van der Veen, and J. P. Woerdman, *Opt. Comm.* **96**, 123, (1993).